MATERIALS CHEMISTRY
FRONTIERS

CHINESE CHEMICAL SOCIETY

ROYAL SOCIETY OF CHEMISTRY

RESEARCH ARTICLE

View Article Online
View Journal | View Issue

Cite this: *Mater. Chem. Front.*, 2025, **9**, 2559

Platinum(II) complexes bearing functionalized NHC-based pincer ligands: synthesis and application in phosphorescent OLEDs†

Purificación Cañadas,[a] Michele Forzatti,[b] Sara Fuertes, *[a] Antonio Martín,[a] Michele Sessolo,[b] Daniel Tordera *[b] and Violeta Sicilia *[c]

Received 15th April 2025,
Accepted 24th June 2025

DOI: 10.1039/d5qm00310e

rsc.li/frontiers-materials

A set of neutral platinum(II) complexes bearing a bis-N-heterocyclic carbene (NHC) pincer ligand with stoichiometry [Pt(C_R*^C^{CN}^C_R*)L] (R = Me (**a**), Et (**b**); L = Cl (**2**), Cbz (**3**), and CN (**4**)) have been prepared. By employing the corresponding bisimidazolium salt (**1a** or **1b**), silver oxide and [PtCl$_2$(cod)] we obtained the Cl derivatives. Then, the subsequent ancillary ligand exchange rendered complexes **3** and **4**. Single-crystal X-ray analysis revealed no Pt–Pt contacts, but some π–π intermolecular interactions within the supramolecular structure of the Cl and CN derivatives. It also showed different crystal packings for the two polymorphs of the Cl complex (**2b**). In diluted solution, photophysical and computational studies disclosed the nature of the low-lying electronic transitions to be mainly ^{3}ILCT [π(C*^C^C*) → π*(C*^C^C*)]/^{3}MLCT [5d(Pt) → π*(C*^C^C*)] for Cl and CN derivatives and L′LCT [π(Cbz) → π*(C*^C^C*)]/L′MCT [π(Cbz) → d(Pt)] for the Cbz counterpart. The blue (**2b**), green (**3b**) and yellowish-orange (**4b**) emissions of 2 wt% PMMA films at λ_{ex} = 370 nm exhibited very high quantum yields (QYs) reaching up to ∼99%. However, at λ_{ex} > 400 nm, in the solid state or in 20 wt% PMMA films, additional structureless low-energy emissions arose from extended structures with a higher degree of aggregation. Complexes **2b–4b** were used as emitters in organic light-emitting diodes (OLEDs), either with a doped or a non-doped emissive layer. Interestingly, and due to their aggregation in extended structures, their emission could be tuned from bluish green to orange just by changing the thickness of the active layers. Devices with **4b** reached a maximum efficiency of 8.08% and a high luminance of 34 071 cd m^{-2}.

Introduction

Technology based on organic light-emitting diodes (OLEDs) is currently at the forefront of applications in full-color display and illumination products.[1,2] The so-called second-generation phosphorescent OLEDs (PhOLEDs) incorporate 3rd-row transition-metal (Ir^{3+}, Pt^{2+}, Os^{2+}, and Au^{3+}) phosphorescent complexes in the emissive layer (EML) to harvest triplet excitons in addition to singlets, raising the theoretical internal quantum efficiency (IQE) from 25% to 100%.[2–4] This is a crucial advantage for future displays, such as virtual reality and automotive panels, which require higher luminance levels, and more efficient and stable devices than those provided by fluorescent OLEDs. Among the three RGB primary colors, green and red PhOLEDs exhibit good performance in terms of efficiency and stability, but the development of stable and efficient pure-blue PhOLEDs is still a challenge.[1]

In the chemistry of Pt(II), molecular design, mainly of the chromophoric ligand, plays a key role in the development of efficient and stable phosphorescent complexes.[4,5] In this sense, bidentate and tridentate cyclometalated N-heterocyclic carbenes (C^C* and C*^C^C*)[4,6] induce a large HOMO–LUMO gap, at least of 2.8 eV required for blue emitters. Besides, their strong field nature, which pushes up the dd* states, and their rigidity, which hinders severe geometrical distortions of the complexes upon excitation, preclude nonradiative deactivation and bond-breaking processes. Therefore, Pt(C^C*) and Pt(C*^C^C*) are excellent platforms to get blue phosphorescent complexes. However, it requires the presence of strong electron-withdrawing substituents in the aromatic fragment

---

[a] Departamento de Química Inorgánica, Facultad de Ciencias, Instituto de Síntesis Química y Catálisis Homogénea (ISQCH), CSIC – Universidad de Zaragoza, Pedro Cerbuna 12, 50009, Zaragoza, Spain. E-mail: s.fuertes@csic.es

[b] Instituto de Ciencia Molecular, Universidad de Valencia, C/Catedrático J. Beltrán 2, 46980, Paterna, Spain. E-mail: daniel.tordera@uv.es

[c] Departamento de Química Inorgánica, Escuela de Ingeniería y Arquitectura de Zaragoza, Instituto de Síntesis Química y Catálisis Homogénea (ISQCH), CSIC – Universidad de Zaragoza, Campus Río Ebro, Edificio Torres Quevedo, 50018, Zaragoza, Spain. E-mail: sicilia@unizar.es

† Electronic supplementary information (ESI) available. CCDC 2431931–2431934. For ESI and crystallographic data in CIF or other electronic format see DOI: https://doi.org/10.1039/d5qm00310e

involved in the HOMO.[6] Otherwise, the emission shifts to the sky-blue or green spectral range. Additionally, these planar complexes with extended π-systems tend to establish π–π and/or Pt···Pt interactions with adjacent molecules in the solid state or even dispersed in films at high wt%. This happens in the absence of bulky substituents that hinder excimer/aggregate formation,[7] and in these cases, the emission shifts to lower energies, appearing in the yellow, orange or red spectral range.[4] Driven by the stability of this class of compounds and their photoluminescence color tunability, some of them have been used as active materials in the EML of PhOLEDs.

In this sense we recently published OLEDs based on the compounds [Pt(Cbz-C^C*$_{bzim/im}$)(L^L)] (HC^C*$_{im}$ = 1-(4-(9*H*-carbazol-9-yl)phenyl)-3-methyl-1*H*-imidazol-2-ylidene, HC^C*$_{bzim}$ = 1-(4-(9*H*-carbazol-9-yl)phenyl)-3-methyl-1*H*-benzimidazol-2-ylidene; L^L acetylacetonate, 2-diphenylphosphinobenzoate, 2-diphenylphosphinophenolate). The best performing devices were obtained for [Pt(Cbz-C^C*$_{bzim}$)(acac)] and [Pt(Cbz-C^C*$_{bzim}$)(2-diphenylphosphinobenzoate)] in ultrathin non-doped emissive layers. They showed green EL derived from aggregates with a turn-on voltage of 2.99 V and 2.55 V, a peak luminance of 39 208 and 25 837 cd m^{-2} and a peak current efficiency of 44.9 and 40.0 cd A^{-1} (12.8% and 13.4% EQE), respectively.[8] A revision of complexes tested in OLEDs containing a Pt(C^C*) system is included there.[8] Complexes used in PhOLEDs containing Pt(C*^C^C*) chromophores are represented in Fig. 1.

Li, Fleetham *et al.* reported the first complex bearing a pincer C*^C^C* fragment used as an active material in PhOLEDs, **CCC1**. It yielded pure-blue EL (CIE coordinates: 0.16, 0.13) and good performance, reaching an EQE$_{max}$ of 15.7%.[9] The same group used **CCC1** as a single dopant to get white light (CIE coordinates: 0.33, 0.33) combining the emission from monomers and excimers, reaching an EQE$_{max}$ of 18.2% at 10 wt%.[10] Blue EL was also achieved by C. M. Che *et al.* using **CCC2** (CIE$_{xy}$: 0.14, 0.23) and **CCC3** (CIE$_{xy}$: 0.15, 0.11) with improved performances: EQE$_{max}$ 19.9% and 22% respectively.[11] **CCC4** has been recently reported by Zhu, Lee and co-workers, and was employed as a dopant sensitizer for a narrow band MR-TADF terminal emitter: ν-DABNA. Using this strategy, they obtained hyperphosphorescent pure-blue OLEDs with EQEs of up to 33.59%, and CIExy of (0.12, 0.15).[12] Finally, with **CCC5** Bräse, Wang *et al.* were able to tune the emission of monomers and excimers to get single-doped WOLEDs with CIE coordinates of (0.32, 0.36), a color rendering index (CRI) of over 83, and an EQE$_{max}$ of 24.4%.[13]

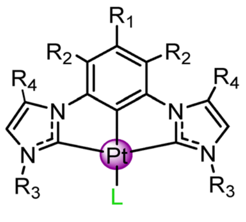

CCC1: $R_1 = R_2 = R_4 = H$, $R_3 = Me$, L = Cl pure blue and white
CCC2: $R_1 = R_2 = R_4 = H$, $R_3 = nBu$, L= $CNB(C_6F_5)_3$ blue
CCC3: $R_1 = CF_3$, $R_2 = R_4 = H$, $R_3 = nBu$, L= $CNB(C_6F_5)_3$ pure blue
CCC4: $R_1 = tBu$, $R_2 = R4 = H$, $R_3 = iPr$, L= Cl blue
CCC5: $R_1 = R_3 = R_4 = Me$, $R_2 = H$, L = Cl sky blue, white

Fig. 1 Complexes used in PhOLEDs containing Pt(C*^C^C*) chromophores.

Keeping in mind all of the above and our previous contribution to blue/green-emitting Pt(II) complexes bearing bidentate cyclometalated NHCs,[14] we decided to address the synthesis of a new functionalized pincer ligand with an electron-withdrawing pendant group (CN) in the aryl ring. Several Pt(II) complexes derived from it have been prepared and fully characterized. The study of their photophysical properties with the aid of DFT and TD-DFT calculations was addressed before their use as active materials in PhOLEDs.

Results and discussion

Synthesis and characterization of new NHC-based pincer type ligands and neutral platinum(II) complexes [Pt(C*^C^{CN}^C*)L]

1,1′-(5-Cyano-1,3-phenylene)bis(1*H*-imidazole) (**A**), the bisimidazolium salts, [C*$_R^C^{CN}$^C*$_R$]I$_2$ (R = Me **1a**, Et **1b**), and the platinum(II) complexes [Pt(C$_R$*^C^{CN}^C$_R$*)Cl] (R = Me **2a**, Et **2b**), [Pt(C$_R$*^C^{CN}^C$_R$*)Cbz] (R = Me **3a**, Et **3b**, Cbz = 9*H*-carbazolate) and [Pt(C$_R$*^C^{CN}^C$_R$*)CN] (R = Me **4a**, Et **4b**) were prepared as indicated in Scheme 1. More details are provided in the Experimental section in the ESI.† When employing the bisimidazolium salt **1a**, [PtCl$_2$(cod)], as the platinum precursor, and silver oxide as deprotonating and transmetalating agent, the chloride platinum complex **2a** was obtained after work up of the reaction mixture (see the Experimental section, ESI†). The protocol to obtain **2a** has been slightly modified with respect to our previously reported ones for bidentate C^C* derivatives,[15,16] and also differs from those used by other authors,[9,11,12,17] reaching higher reaction yields. The chloride ligand in complex **2a** could be replaced by carbazolyl and cyanide rendering complexes **3a** and **4a** respectively. To increase the solubility of these species and allow their characterization in solution, we prepared the bisimidazolium

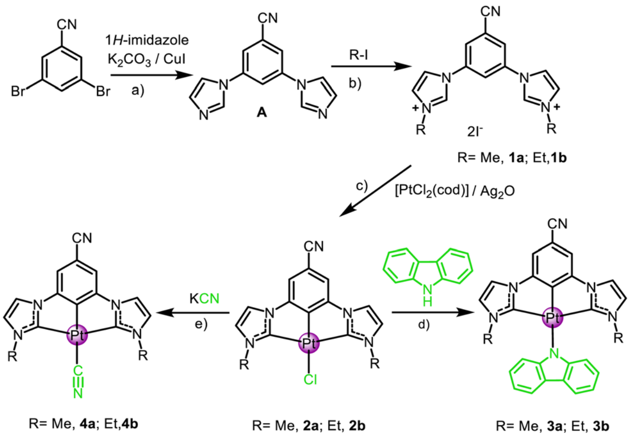

a) DMF, Ar, 140 °C, 24h; b) MeCN, Ar, Δ, 48h; c) dark, DMF, Ar, 165 °C, 18h; d) i: ^{t}BuONa/30′, rt; ii: THF, overnight, rt; e) acetone/MeOH, rt, overnight

Scheme 1 Synthesis of bis-NHC pincer ligands and Pt^{II} complexes.

Table 1 Relevant NMR data (δ(ppm), *J*(Hz))

	δPt{^{1}H}	$^4J_{Pt,HPh}$	δMe(im)	δEt(im)	δC*	$^1J_{Pt-C*}$ [c]
1a[a]			4.01			
1b[a]				4.35, 1.55		
2a[a]	−3998	16.4	4.14		171.8	1152.2
2b[b]	−4013	16.8		4.76, 1.50	173.2	1140.3
3a[b]	−4119	12.6	2.86		174.8	1165.0
3b[b]	−4107	12.6		3.20, 0.60	173.0	1176.2
4b[b]	−4553	10.6		4.62, 1.55	171.1	1130.1

[a] DMSO-d_6. [b] CD_2Cl_2. [c] $^1J_{Pt-C*}$ were determined using $^1H-^{13}C$ HMBC.

salt **1b**, with an Et group instead of Me in the NHC-wingtip and from that, the platinum(II) complexes **2b–4b**.

The $^4J_{Pt,HPh}$ is also sensitive to the ancillary ligand (Table 1), becoming smaller as its *trans* influence became greater ($Cl^- < Cbz^- < CN^-$). It is also worth noting the important upfield shift undergone by the resonances of the Me and Et groups on the imidazole fragments in complexes **3a/3b**. This effect has been associated with the anisotropic shielding effect caused by the proximity in space of the aromatic ring current of the Cbz to them.[18] Regarding the $^{13}C\{^1H\}$ NMR spectra, the C_{NHC} (hereafter referred to as C*) resonances appear at $\delta > 170$ ppm with ^{195}Pt coupling constants of 1130–1176 Hz, in agreement with the existence of a σ Pt–C* bond.

The proposed structures on the basis of the NMR data were confirmed *via* X-ray diffraction analysis of **2b**, **3b** and **4b** (Fig. 2 and Fig. S10, ESI†). Crystals of **2b** were obtained in two polymorphic forms by slow diffusion of methanol into a saturated solution of DMF (**2b** and **2b·H$_2$O**). The asymmetric unit of **3b** contains two molecules (Pt1 and Pt2) with similar structural details. Selected bond lengths and angles are summarized in Table 2. In these complexes, the Pt^{II} center exhibits a distorted square-planar coordination environment, with C*–Pt–C* angles of ∼157°. These angles and the Pt–C bond lengths are very similar to those observed in other Pt^{II} complexes bearing dicarbene pincer ligands.[11,12,17,19] In **3b**, the plane of the carbazolyl ligand is almost perpendicular to that of the molecular plane (Pt1, C1, C6, C13, N6/Pt2 C42 C35 C30 N12) with a dihedral angle of 84.55(14)°/83.77(15)° to minimize the steric repulsions. Further inspection of the crystal packing of all complexes revealed that there are no Pt–Pt contacts; but some π–π (*ca.* 3.49, 3.43 Å) and Pt–π offset interactions in **2b·H$_2$O** and **4b·H$_2$O**. In them, the molecules stack into 1D-staggered chains (see cyan dotted lines in Fig. 2b for **2b·H$_2$O** and Fig. S10 for **4b·H$_2$O**, ESI†). Both crystal packings show the same type of lone pair $d_{z^2}[M^{II}]$–π interactions,[12,20,21] with the Pt center pointing to the imidazole ring and located at the distance of 3.46 Å (**2b·H$_2$O**) and 3.44 Å (**4b·H$_2$O**), which is slightly smaller than the sum of the van der Waals radii (RvdW(Pt) + RvdW(C) = 3.47 Å).[22,23] The extended structure is almost identical in both and is also supported by a crystallization water molecule that bridges neighboring Pt complexes (black dotted lines) *via* hydrogen bonding interactions with the ancillary ligand (*d* C≡N···O: 2.930(2) Å **4b·H$_2$O**, *d* Cl···O: 3.178(2) Å **2b·H$_2$O**)

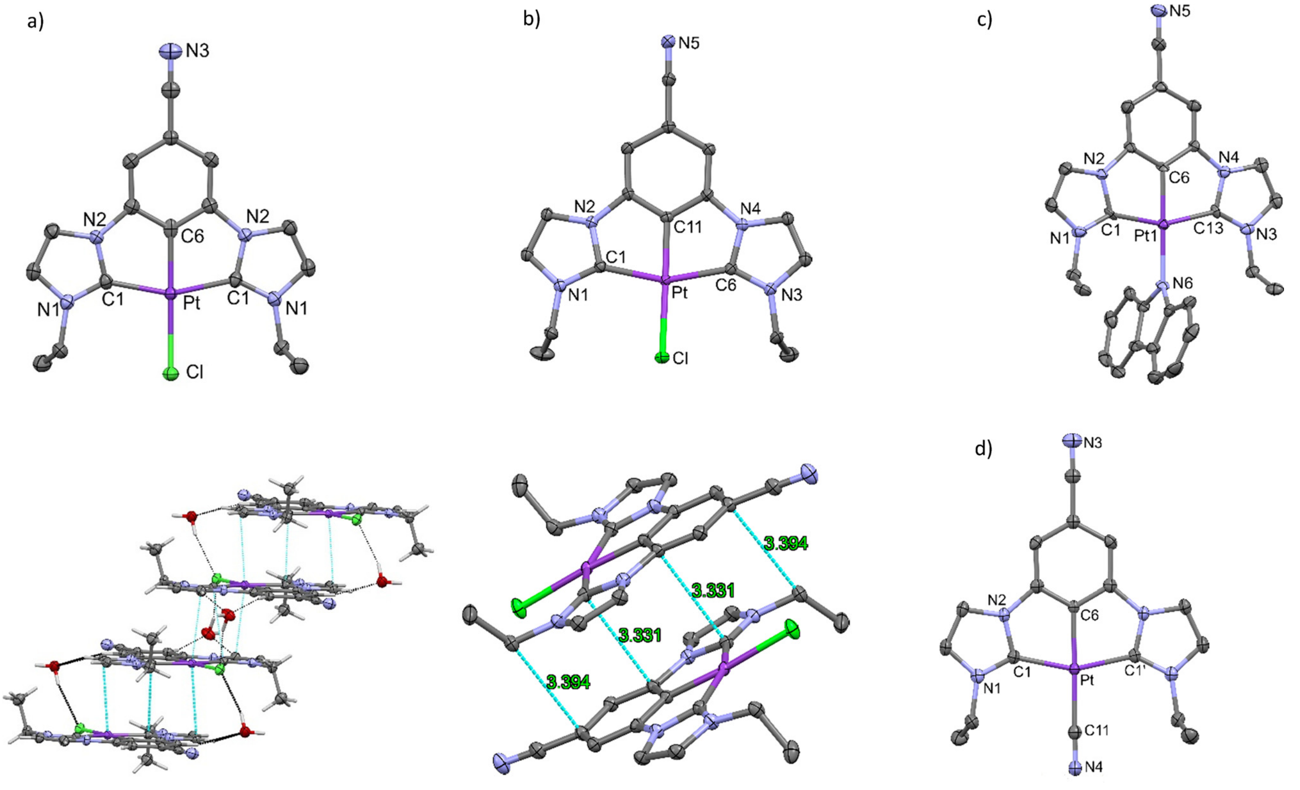

Fig. 2 X-ray crystal structures and supramolecular structure view of **2b·H$_2$O** (a) and **2b** (b), and X-ray crystal structures of **3b** (c) and **4b·H$_2$O** (d). Thermal ellipsoids are drawn at the 50% probability level. Hydrogen atoms and solvent molecules have been omitted for clarity.

Table 2 Selected X-ray data for Pt complexes

	2b L = Cl	**2b·H$_2$O** L = Cl	**3b** (Pt1/Pt2) L = N$_{Cbz}$	**4b·H$_2$O** L = C$_{CN}$
Bond lengths (Å)				
Pt–C*	2.037(2) 2.028(2)	2.038(3)	2.011(7)/2.028(6) 2.030(6)/2.037(6)	2.029(4)
Pt–C$_{ph}$	1.938(2)	1.961(6)	1.956(6)/1.947(6)	1.992(4)
Pt–L	2.3857(5)	2.4057(13)	2.100(5)/2.089(5)	2.018(4)
C–N	1.151(3)	1.157(7)	1.150(9)/1.511(10)	1.137(6)
C11–N4				1.154(6)
Bond angles (°)				
C*–Pt–C$_{ph}$	78.99(8) 78.74(8)	78.89(10)	79.4(2)/78.6(3) 78.4(3)/79.1(2)	78.38(9)
C*–Pt–L	100.20(6) 102.11(6)	101.11(10)	100.4(2)/100.2(2) 101.8(2)/102.0(2)	101.62(9)
C*–Pt–C*	157.69(8)	157.8(2)	157.8(3)/157.7(3)	156.76(18)

and *via* C$_{sp^2}$–H···O interactions with the C*^C^C* group (*d* C···O: 3.296(5) Å **4b·H$_2$O**, 3.273(4) Å **2b·H$_2$O**). However, in **2b**, the Pt molecules do not stack into infinite 1D-chains; they arrange in pairs, in a head to tail fashion, through π–π interactions (*ca.* 3.331 Å, Fig. 2d).

Photophysical properties and theoretical calculations

Absorption properties. Due to the low solubility of the methyl derivatives (**2a–4a**) and considering that the UV-Vis spectra of **2a** and **2b** are almost identical (Fig. S11, ESI†), we only carried out the absorption study of the ethyl derivatives. UV-Vis absorption spectra of complexes **2b–4b** in dichloromethane at low concentrations (5 × 10^{-5} M) are depicted in Fig. 3 and their data listed in Table S2 (ESI†). They all show intense absorptions at λ < 300 nm and weaker vibronic ones in the range of 350–400 nm, which are normally attributed to ^{1}IL π–π* [(C*^C^C*)] and ^{1}IL/^{1}MLCT [dπ(Pt)/π(C*^C^C*) → π*(C*^C^C*)], respectively.[11,12,17] Substitution of the chloride ligand by CN has hardly any effect on the absorption spectra; however, the carbazole group increases the absorptivity and produces an additional low-lying absorption (λ: 460 nm, inset of Fig. 3). This low energy band can be assigned to excited states ^{1}L′LCT [π(carbazole) → π*(C*^C^C*)] in nature, as found in related metal–carbazolyl complexes.[24–26] The lowest energy absorptions for **2b** (λ = 373 nm) and **3b** (λ = 459 nm) obey Beer's law in the concentration range from 10^{-6} to 10^{-3} M (Fig. S12 and S13, ESI†), which indicates the absence of significant ground state aggregation.

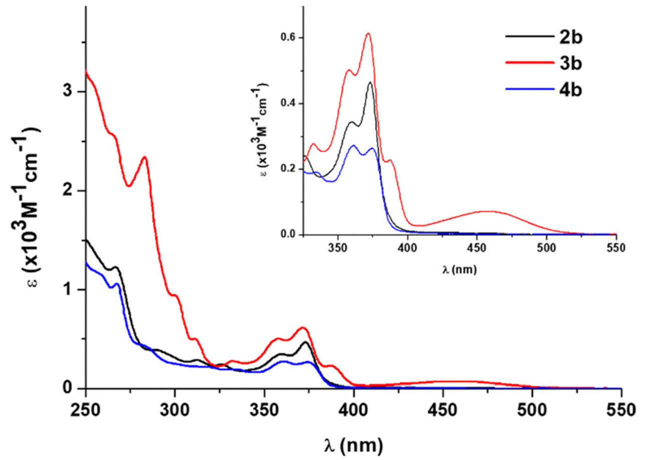

Fig. 3 UV-vis absorption spectra in CH$_2$Cl$_2$. Inset. Expanded view of the low energy region.

To better understand their photophysical properties, density functional theory (DFT) and time dependent-DFT (TD-DFT) calculations were carried out at the M06/SDD(Pt)/6-31G*(ligand atom) level. The geometries of the S$_0$ and T$_1$ were optimized with no restrictions; see the Experimental section (ESI†) for further details. The frontier orbitals (FOs) involved in lowest energy absorptions have been represented in Fig. 4. As can be seen, in CH$_2$Cl$_2$, the calculated S$_1$ transition is mainly a HOMO → LUMO one (Table S3, ESI†). The analysis of the frontier orbitals (Table S4, ESI†) revealed that for **2b** and **4b**, the HOMO is mainly centered on the C*^C^C* (≥50%) ligand and the platinum center (~30%) and also on the Cl (15%) atom for complex **2b**, while for **3b**, the HOMO is essentially located on Cbz (91%). However, the LUMO is almost the same for all three complexes, with a great participation of the C*^C^C* (~75%) and the Pt center (~25%). Thus, the lowest energy absorption, S$_1$, would be mostly attributed to a mixed ILCT/MLCT transition for **2b** and **4b**, whereas L′LCT [π(Cbz) → π*(C*^C^C*)]/L′MCT [π(Cbz) → d(Pt)] for **3b**, confirming the early assignment made in the UV-Vis section. By comparing the calculated data corresponding to the Cl (**2b**) and CN (**4b**) complexes, they reveal that although the CN ancillary ligand does not formally contribute to the FOs, it stabilizes them due to its electron-accepting nature, causing a subtle change in the HOMO–LUMO gap with respect to that in the Cl complex. The Cbz group in **3b** has a greater effect on the HOMO–LUMO gap; its good electron-donating ability fully changes the nature of the HOMO and increases its energy, while it does not modify the LUMO with respect to those of **2b** and **4b**, decreasing the HOMO–LUMO gap appreciably (Fig. 4).

Emission properties

The emission properties of the C$_{Et}$*^C^{CN}^C$_{Et}$* derivatives **2b–4b** were studied in CH$_2$Cl$_2$ solutions, PMMA films and in the solid state; those of complex **2a** were measured to evaluate the effect of the smaller Me against Et in the imidazole fragments. The collected data have been summarized in Table 3. In diluted CH$_2$Cl$_2$ solution (5 × 10^{-5} M) at r.t. under an Ar atmosphere (Fig. 5a and Fig. S14, S15 in the ESI†), compounds with non-bulky ancillary ligands, Cl (**2a**, **2b**) and CN (**4b**), display a bright phosphorescence emission with maxima in the blue spectral region (λ_{max} ~ 460 nm) and a monoexponential decay of ≈ 2 μs (Fig. S16, ESI†). The emission spectrum of **2a** (Fig. S14, ESI†) in CH$_2$Cl$_2$ solution matches that of **2b**, so the presence of Me or Et in the NHC-wingtip does not seem to affect the emissive state of these complexes.

All complexes **2a**, **2b** and **4b** exhibit, in addition, an emerging low energy emission at λ > 600 nm. We observed that for **4b** it becomes much more intense with increasing concentration (see Fig. S15, ESI†) and exhibits a monoexponential and shorter decay time than the high energy one. For **2b**

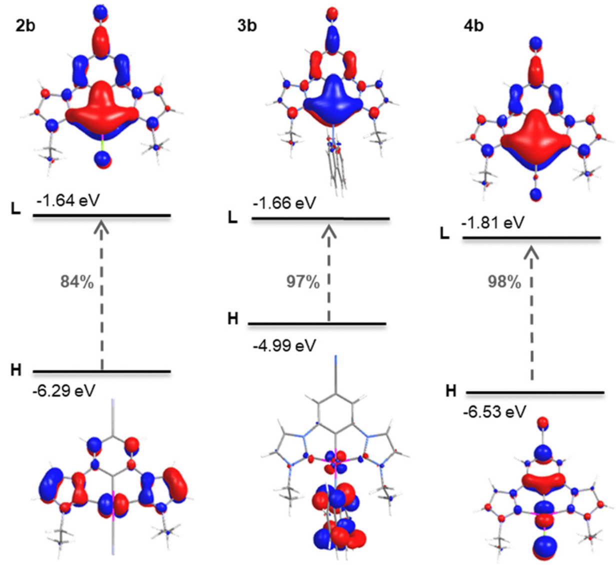

Fig. 4 Frontier molecular orbital distributions for **2b–4b** and contribution of the HOMO → LUMO transition to the S_1.

(Fig. S14, ESI†) and **4b** the excitation spectra of the high and low-energy bands match one another and resemble their UV-vis spectra. Therefore, in all cases, an excimeric origin of the low-energy emission band can be presumed. The structured shape of the high-energy bands (λ_{max} ∼ 460 nm) with vibrational spacing [1100–1400 cm^{-1}] corresponding to C=C/C=N stretching of the organic ligand suggests a pronounced ^{3}IL nature of these emissions. Considering that in each case the excitation spectrum and the lower energy absorption match one another, the emission can be attributed to a mixed ^{3}ILCT [π(C*^C^C*) → π*(C*^C^C*)]/^{3}MLCT [5d(Pt) → π *(C*^C^C*)] excited state, in agreement with the emission lifetimes and the spin density distributions calculated for the T_1 states. As shown in Fig. S17 (ESI†), these are mainly located on the C*^C^C* ligand (1.680 **2b** and 1.755 **4b**) and to a smaller extent on the Pt center (0.290 **2b** and 0.215 **4b**) and the ancillary ligands (0.030 **2b** and 0.030 **4b**). This contribution of the Pt orbitals could explain to some extent the small value of the emission decay ($\tau \sim 2$ μs). By contrast, the incorporation of the Cbz as an ancillary ligand (**3b**) results in a structureless emission band at 590 nm, clearly shifted to lower energy with respect to those for **2b** and **4b**. This fact is explained by the different nature of the lowest energy excited state, L′LCT [π(Cbz) → π*(C*^C^C*)]/L′MCT [π(Cbz) → d(Pt)], in accordance with calculated spin density distributions (Cbz: 0.860, C*^C^C*: 0.821, Pt: 0.319). In rigid media, especially in a 2 wt% PMMA film, the emission of **3b** undergoes a clear hypsochromic shift (1672 cm^{-1}, from 590 nm in solution to 537 nm in the film) and a significant narrowing of the full width at half maximum (FWHM) from 107 nm (3028 cm^{-1}) in solution to 68 nm (2273 cm^{-1}) in the film; along with an increase in the quantum yield and lifetime values (see Fig. 5b and Table 3). This luminescence rigidochromism is characteristic of the mixed charge transfer excited state,[27–29] in accordance with a L′LCT/L′MCT assignment, in view of the match between excitation and absorption spectra.

The emission behaviour in rigid media of **2b** and **4b**, with non-bulky ancillary ligands, greatly differs from that of **3b**, as observed before in solution. In PMMA films at low doping concentrations (2 wt%), **2b** shows an emission whose profile depends on the excitation wavelength (see Fig. 6). When excited at $\lambda \leq 370$ nm, **2b** shows a vibronic band peak at 465 nm, similar to the one obtained in solution, together with an incipient low energy emission at $\lambda > 600$ nm. The latter becomes the maximum when $\lambda_{ex} > 400$ nm at any doping concentration, 2 wt% or 20 wt% (Fig. S18, ESI†), and is the only emission band observed in the solid state (Fig. 7).

As previously discussed, the blue vibronic emission resembles that measured in solution, but reaches higher quantum yield (>90%), microsecond lifetimes and high radiative constants (>10^5 s^{-1}, see Table 3); thus we assume the same origin

Table 3 Photophysical data of Pt complexes at room temperature under an Ar atmosphere

Comp.	Medium	λ_{exc} (nm)	λ_{em} (nm)	τ (μs) [λ_{em}]	Φ (%)	$k_r \times 10^5$ (s^{-1})	$k_{nr} \times 10^5$ (s^{-1})	CIE (x, y)
2a	CH_2Cl_2[a]	370	462_{max}, 494, 525_{sh}	2.0 [462]	21	1.05	3.95	0.17, 0.26
	Solid	520	700	0.5, 1.3	23	1.77	5.92	0.65, 0.34
2b	CH_2Cl_2[a]	370	463_{max}, 495, 525_{sh}	2.3 [463]	28	1.22	3.13	0.20, 0.27
	$2wt\%_{PMMA}$	370	464_{max}, 494, 525_{sh}	6.1 [464]	98	1.60	0.03	0.17, 0.26
		410	465, 494, 615_{max}	6.3, 1.7 [615]	49	0.78	0.81	0.40, 0.35
	$20wt\%_{PMMA}$	370	464_{max}, 494, 615	5.0, 1.8 [464]	75	1.50	0.50	0.37, 0.35
		410	464, 494, 615_{max}	1.6 [615]	55	3.43	2.81	0.51, 0.39
	Solid	470	620	0.6, 1.4	16	1.14	6.00	0.54, 0.43
3b	CH_2Cl_2[a]	370	590	0.8	30	3.75	8.75	0.52, 0.46
	$2wt\%_{PMMA}$	470	537	1.9	76	4.00	1.26	0.37, 0.60
	Solid	500	575	0.8	33	4.12	8.37	0.49, 0.49
4b	CH_2Cl_2[a]	370	461_{max}, 494, 525_{sh}	1.1 [461]	10	0.91	8.18	0.20, 0.28
	CH_2Cl_2[b]	370	461_{max}, 494, 525_{sh}, 610	0.8 [610]	14	1.75	10.75	0.40, 0.34
	$2wt\%_{PMMA}$	370	461, 494, 600_{max}	1.5 [600]	99	6.60	0.06	0.47, 0.41
	$20wt\%_{PMMA}$	370	460, 494, 600_{max}	1.3 [600]	75	5.77	1.92	0.53, 0.42
		480	600_{max}, 680_{sh}	1.2, 0.3 [600]	67	5.58	2.75	0.58, 0.41
	Solid	470	611	1.9, 0.6	66	3.47	1.79	0.58, 0.41
		550	695	2.6, 0.5	48	1.85	2.00	0.64, 0.35

[a] Measured at 5×10^{-5} M. [b] Measured at 5×10^{-4} M; $k_r = \Phi_{PL}/\tau$, $k_{nr} = (1 - \Phi_{PL})/\tau$.

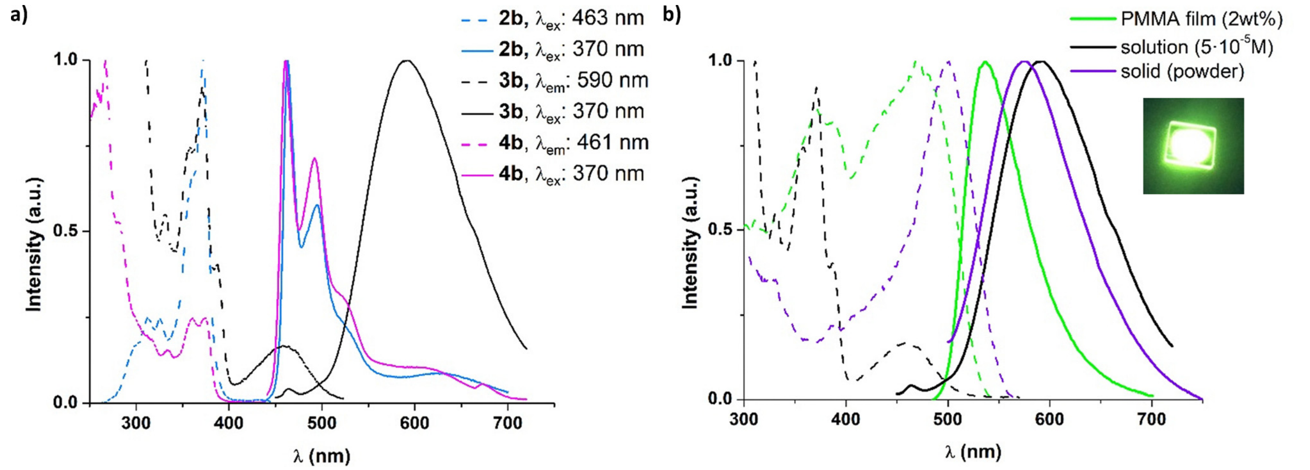

Fig. 5 (a) Normalized excitation (---) and emission (—) spectra of **2b–4b** in CH_2Cl_2 solution (5 × 10^{-5} M) at r.t. (b) Normalized excitation (—) and emission (—) spectra of **3b** in different media. Picture of the 2 wt% PMMA film under 365 nm light.

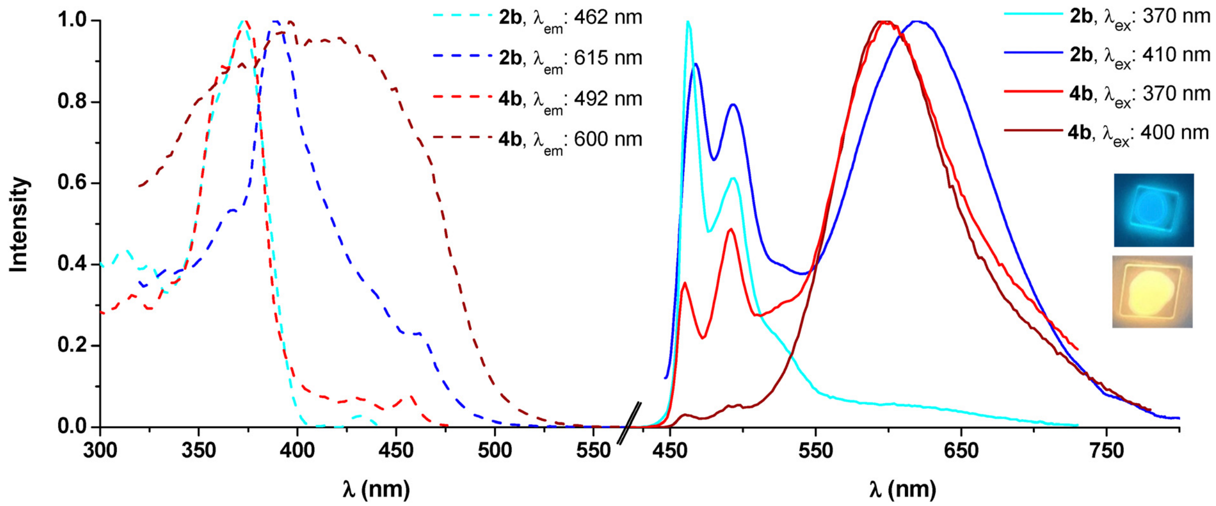

Fig. 6 Normalized excitation (----) and emission (–) spectra of in 2 wt% PMMA film. Pictures of **2b** (blue emitter film) and **4b** (yellowish-orange emitter film) under 365 nm light.

(^{3}ILCT [π(C*^C^C*) → π*(C*^C^C*)]/^{3}MLCT [5d(Pt) → π*(C*^C^C*)]). However, the Gaussian shaped low-energy emission is probably due to existing aggregates in the ground state, in view of the different excitation spectra obtained for the high and low energy bands. The planarity of this molecule and its extended π system are responsible for the tendency to form aggregate structures involving Pt–Pt and π–π intermolecular interactions,[30] even at low Pt complex loadings, like in analogous complexes [Pt(C_{NHC}^C_{Ar}^C_{NHC})L] (L = Cl, CN).[11,12] As a result, in **2b** the emission color can be modified from blue to white (neutral and warm) and up to orange, by changing the doping concentration in PMMA films or the excitation wavelength, as illustrated by the chromaticity diagram shown in Fig. S19 (ESI†). It is worth noting that compound **2b** can provide white photoluminescence (Table S5, ESI†) with high QY, correlated color temperatures (CCT) ranging from 1990 to 4159 K, acceptable color rendering index (CRI) values of 78–67 and CIE coordinates close to the Planckian locus ($|D_{uv}| \leq 0.006$, 20 wt%, Table S5, ESI†). Hence, these photometric and colorimetric parameters are fairly close to the values reported for single-doped WOLEDs based on square-planar Pt(II) complexes,[13,31–35] and comply with the stipulated values for indoor solid-state illumination.[36,37]

For **4b** in PMMA films, at any doping concentration (2 wt%, 20 wt%), the emission at λ_{max} ~ 600 nm, due to aggregates, is the most important or the only one, when exciting at wavelengths > 400 nm (Fig. 6 and Fig. S20, ESI†). In the solid state, the emission profile of **4b** depends on the excitation wavelength (Fig. 7). In this case, upon excitation with λ_{ex} > 500 nm, an additional and new structureless emission band appears at λ_{em} = 695 nm. This can be attributed to heterogeneity in the solid and the formation of higher degree aggregates, in view of the different packing arrangement possibilities observed for these kinds of complexes. In fact, both excitation and emission

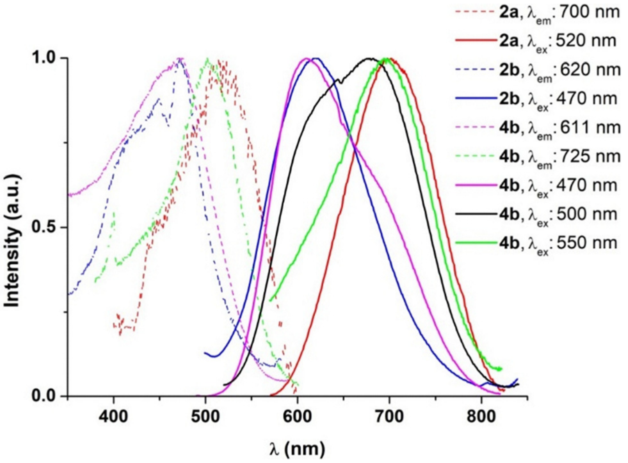

Fig. 7 Normalized excitation (---) and emission (–) spectra in the solid state.

spectra are comparable to those obtained for **2a**, with a methyl substituent in the imidazole fragments (Fig. 7). Thus, compounds **4b** and **2a** present a great tendency to form aggregates involving close and extended Pt···Pt/π···π interactions.

Organic light emitting diodes

Next, complexes **2b**, **3b** and **4b** were used as emitters in organic light-emitting diodes (OLEDs). With the goal of fabricating OLEDs with emitter aggregation induced tunable emission and given that the photoluminescence properties of compounds **2b** and **4b** change significantly depending on the medium, we focused on these two emitters in our study. In order to process the active layer, there are two main approaches. The first and more common approach consists in co-evaporating the emitter alongside a host, yielding a doped emissive layer. Alternatively, the emitter molecules can be inserted into the device's stack as sub-monolayers, by keeping the amount of deposited material low (nominal thickness <1 nm). We decided to adopt this second strategy as it simplifies the fabrication process and reduces material consumption,[38] and it could allow for a simple and fast method of tuning the emission *via* changing the thickness of the active layer.

The selected device architecture was ITO (150 nm)/PEDOT:PSS (35 nm)/TAPC (20 nm)/mCP (10 nm)/Pt(II) complex/PO-T2T (45 nm)/Ba (3 nm)/Ag (100 nm). PEDOT:PSS (poly(ethylenedioxythiophene):poly(styrenesulfonate)), TAPC (1,1-bis[(di-4-tolylamino)phenyl]cyclohexane), mCP (1,3-bis(*N*-carbazolyl)benzene), and PO-T2T (2,4,6-tris[3-(diphenylphosphinyl)phenyl]-1,3,5-triazine) were employed as the hole-injection, hole-transport, exciton-blocking, and electron-transport materials, respectively. Ba and Ag were used for the electron injection layer and the cathode, respectively. All layers, except for PEDOT:PSS, were deposited through thermal evaporation (for further details, refer to the Experimental section, ESI†). The transport layers were selected according to their compatible energy levels with the studied emitters (Fig. S21a and b, ESI†). The frontier orbital energies of the emitters were measured by means of photoelectron spectroscopy (PESA) in air (Fig. S22a–c and Table S6, ESI†). The emissive layer (EML) consisted of a non-doped layer of either **2b** or **4b**. To probe the effect of the dispersion level on the emission properties of the emitters, 6 different thickness values were studied, namely 3 nm, 1 nm, 0.3 nm, 0.1 nm, 0.03 nm and 0.01 nm. It is important to note that at these thickness ranges, the molecules stop forming a neat continuous layer but are rather dispersed on the layer underneath: the lower the nominal thickness, the lower the amount of emitter molecules being deposited and the higher the average intermolecular distance.[39] The stability of the active materials under 315 °C was initially checked by TGA analysis. It was also proved under vacuum deposition conditions (heating up to 250 degrees at a base pressure of 10^{-6} mbar) since comparison of the NMR spectrum of the remaining powder with the reference confirmed no sign of degradation (see Fig. S23, ESI†).

Emission from OLEDs with **2b** was observed regardless of the EML thickness. However, both the turn-on voltage (that is, the voltage value at which the emission starts, reported here at a luminance of 1 cd m^{-2}) and the color varied significantly across devices with different thickness values. For instance, for values in the range 0.01–0.3 nm the devices only turn on past 3 V and have a bluish-green color (Fig. S24, ESI†). The devices with an EML thickness of 1 nm turned on at 2.8 V and showed green color, while those with an EML of 3 nm turned on already starting from 2.2 V and appeared yellow. Despite these differences in color, the electroluminescence (EL) spectra of all devices could be described as a combination of the same 4 peaks (Fig. 8a). The highest energy peak is centered at 470 nm and is analogous to the high energy emission visible in the PL spectrum of the compound when measured in either CH_2Cl_2 or PMMA. However, unlike what is observed in the PL, here it is never the most intense peak. While it is clearly visible for thickness values in the range 0.01–0.3 nm, its intensity decreases significantly for higher thicknesses (1 nm) and completely disappears at 3 nm (Fig. S25, ESI†). The second peak is centered at 501 nm and is the most intense peak for thicknesses in the range of 0.01–0.3 nm. The peak is also visible for the 1 nm devices (albeit only as a shoulder to the lower energy peak) and is, once again, absent for 3 nm. The third peak is centered at around 530 nm, but in the range 0.01–0.3 nm, it is only present as a shoulder to the main 501 nm emission. Interestingly, this shoulder is most intense for 0.01 nm, even though it also partially depends on the applied voltage (as this peak tends to become weaker as the voltage is raised, Fig. S26, ESI†). These first three peaks are also all visible in the PL spectrum of **2b**, with the same vibrational spacing, but all red-shifted by exactly 5 nm in the EL spectrum. The fourth and final peak is only visible for the highest thickness values (1 and 3 nm), even though its presence is noticeable also for 0.3 nm, and red shifts with increasing thickness. In fact, it is centered at 544 nm for 1 nm and 561 nm for 3 nm. This incipient low energy emission is analogous to that observed in the PL spectrum of the compound in rigid media at high doping concentrations or in the solid state.

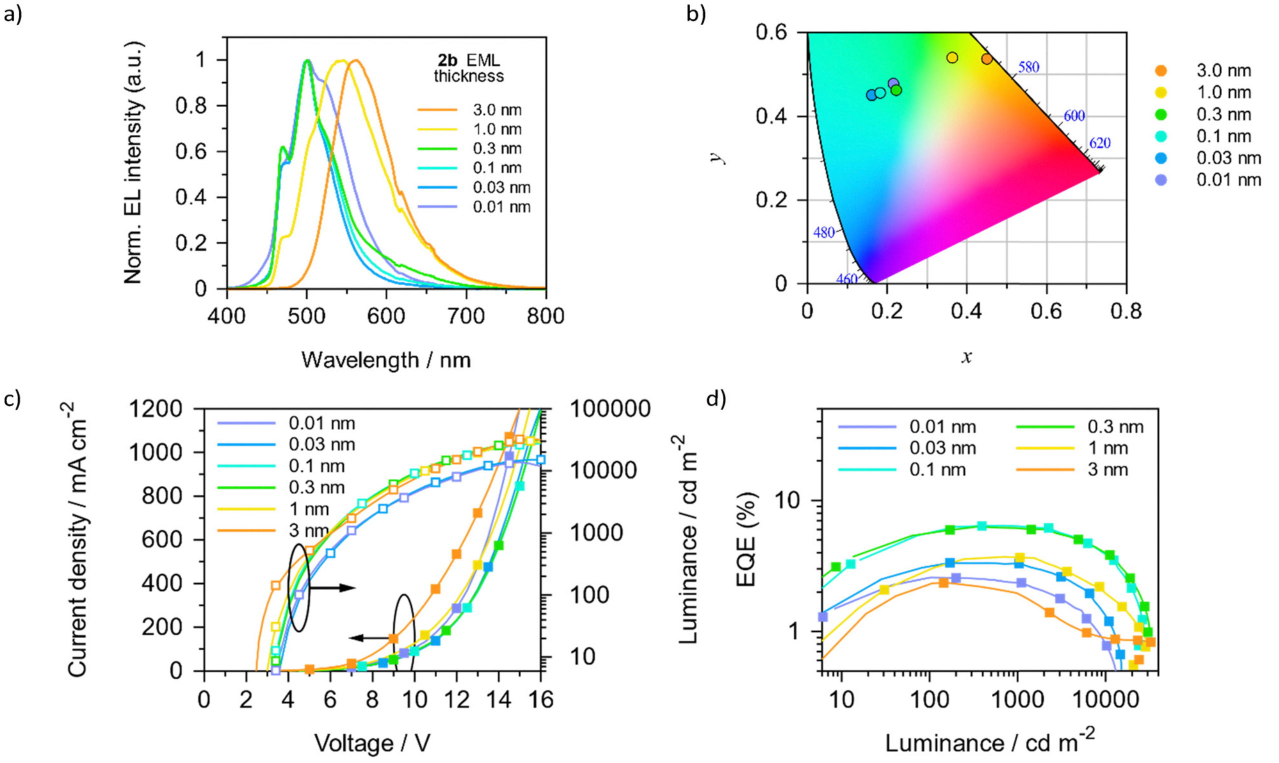

Fig. 8 (a) EL spectra of OLEDs with different thicknesses of the non-doped **2b** emissive layer. (b) Corresponding color points in the CIE chromaticity diagram. (c) *J*–*V*–*L* characteristics and (d) efficiency *vs.* luminance plot for these devices.

As was previously discussed, this emission is expected to come from extended structures involving Pt–Pt and π–π intermolecular interactions, whose abundance increases as the thickness of the non-doped layer surpasses 1 nm where the higher density of molecules on the ultrathin active layer promotes these types of interactions. Hence, the color change across the devices can be attributed to variations in the relative peak intensity and to the shift of the lowest energy peak and is more rigorously quantified in the International Commission on Illumination (CIE) chromaticity diagram (Fig. 8b). Next, the *J*–*V*–*L* characteristics of the devices were measured and are illustrated in Fig. 8c. They show that the maximum brightness increases with increasing thickness, surpassing 30 000 cd m^{-2} in the devices with an EML of thicker than 0.3 nm. The efficiency, on the other hand, only increases with thickness up to 0.1 nm (Fig. 8d), where a peak efficiency of 16.3 cd A^{-1} is reached (corresponding to an external quantum efficiency, EQE, of 6.44%), before starting to decrease again. This trend could be related to the efficiency of the energy transfer from the exciplexes formed by the surrounding layer to the emitter molecules, to the intrinsic emission efficiency of the different predominant species involved for the different dispersion levels and to concentration-related exciton quenching phenomena like TTA.[40,41]

Devices fabricated with **4b** as the emitter have similar spectral properties. In fact, their color also varied from blueish green to orange for increasing thickness values (Fig. S27, ESI†), with the change being due to a variation in the relative intensity of the emission peaks in their EL spectrum (Fig. 9a and Fig. S28 and S29, ESI†), analogous to the behavior observed and discussed in emitter **2b**. The only difference here is that the biggest red shift of the lowest energy excimer emission (565 nm) is already reached at 1 nm and is visible already starting from 0.1 nm. The three higher energy peaks are centered on wavelengths values (470 nm, 499 nm, and 523 nm) that are similar to those observed in the photoluminescence spectra. These observations confirm the greater tendency of this compound to aggregate, when compared to **2b**, and is the reason that the *x* coordinate of the points in the chromaticity diagram reaches slightly higher values (CIE$_{3nm}$ = (0.48, 0.51), Fig. 9b).

There are, however, some differences in the *J*–*V*–*L* characteristics (Fig. 9c). In fact, in the case of **4b**, an increase in thickness decreases the turn-on voltage only up to 0.1 nm, after which it starts to increase again, reaching over 4 V for 3 nm. This might be due to the already mentioned higher tendency to aggregate, which might affect the device conductivity and, in turn, all the electrical properties. Indeed, the same trend is also observed for the luminance and for the efficiency.

The best performing devices, luminance-wise, were those with a 0.1 nm-thick EML, which reached the highest peak luminance among all the devices described in this study (34 071 cd m^{-2}), while the most efficient ones were those with a 0.3 nm-thick EML (22.6 cd A^{-1} and 8.08% EQE), as illustrated in Fig. 9d and summarized in Table S7 (ESI†). Impressively, those devices were able to maintain EQE above 6% even at a very high brightness of 6000 cd m^{-2} and around 4.6% at

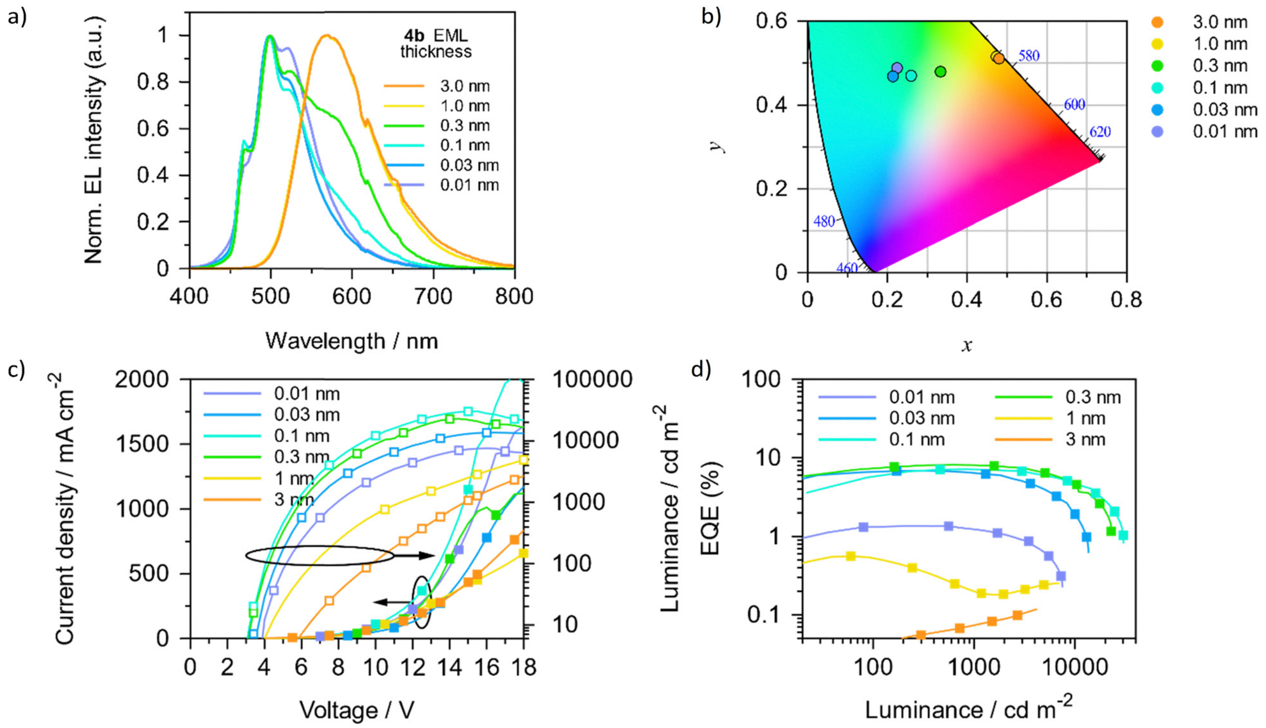

Fig. 9 (a) EL spectra of OLEDs with different thicknesses of the non-doped **4b** emissive layer. (b) Corresponding color points in the CIE chromaticity diagram. (c) *J*–*V*–*L* characteristics and (d) efficiency *vs.* luminance plot for the devices.

10 000 cd m^{-2}, showing a small efficiency roll-off which is of particular interest for display applications. Interestingly, for both **2b** and **4b**, we could tune the emission properties by modifying the thickness of the ultrathin non-doped emissive layer, which balanced the contributions of the vibronic and excimer emission. The selected approach has the advantages of being simple (no co-evaporation required, just a single source), and both fast and cost-effective (as the active layers of the devices are ultrathin).[38]

Besides the EQE and the maximum brightness, the device lifetime is also a very important indicator for practical applications, especially when measured at a high brightness. Therefore, the lifetime of the brightest devices, those with a 0.1 nm-thick non-doped layer of **4b** as the EML, was tested by driving them with a constant current and measuring their luminance *versus* time. Two different current values were employed, which correspond to initial luminance values of 245 cd m^{-2} and 1000 cd m^{-2}, finding device lifetimes LT$_{50}$ of 46 and 11 minutes, respectively (Fig. S30, ESI†). These values are in line with the results obtained for devices with other tetradentate platinum(II) complexes.[2]

As previously described, the use of Cbz as ancillary ligand in **3b** changes the nature of the lowest energy excited state and causes all the emission bands to be red shifted (Fig. 5a). We exploited this property to prepare devices with orange or reddish orange emission using ultrathin undoped EMLs of 1 and 4 nm. In this case, devices turn on showing orange electroluminescence (Fig. S31, ESI†) with an identical EL spectra for the two thickness values (Fig. S30a, ESI†). Consequently, the two devices have the same CIE color coordinates of around (0.56, 0.43) (Fig. S32b, ESI†). However, they possess a different electrical behaviour: devices with an EML thickness of 4 nm achieve a higher luminance with a lower current. The better exciton utilization translates to a higher peak luminance (3107 cd m^{-2}) and efficiency (EQE of 2.74%). At the same time, it was found *via* photophysical measurements that the emission of **3b** undergoes a hypsochromic shift when it is dispersed in a rigid medium rather than in the solid state (537 nm compared to 575 nm, see Table 3 and Fig. 5b). The same effect can be recreated in a light emitting device when dispersing the emitter molecules by inserting them either as an ultrathin layer or as a guest in a dual component EML. We demonstrated this by fabricating OLEDs with the following architecture: ITO (150 nm)/PEDOT:PSS (35 nm)/TAPC (27.5 nm)/CBP:**3b** (9% or 16%, 40 nm)/BAlq (30 nm)/Ba (5 nm)/Ag (100 nm), where CBP is 4,4′-bis(*N*-carbazolyl)-1,1′-biphenyl and BAlq is bis(8-hydroxy-2-methylquinoline)-(4-phenylphenoxy)aluminum. Here, CBP acted as the host material and its choice was based on the emitter frontier orbital energy (Fig. S21c and d, ESI†). TAPC acted as the electron block layer, as its high LUMO level (−2.0 V) helps to confine the electrogenerated triplet excitons within the emissive layer, and BAlq as the electron transport layer. As expected, both devices exhibited identical yellowish-green EL with a peak wavelength of 526 nm with a FWHM of 61 nm (Fig. S33 and S34a, ESI†), corresponding to CIE coordinates of (0.30, 0.64) (Fig. S34b, ESI†). The emission was also stable with increasing driving voltage (Fig. S34c and d, ESI†). The devices with a doping concentration of 16% were more efficient in utilizing excitons, reaching a peak luminance of 18 798 cd m^{-2} (Fig. S34e, ESI†) and a maximum efficiency of 1.55% (Fig. S34f, ESI†).

Conclusions

Bisimidazolium salts with a cyano substituent in the phenylene ring, $[C^*{}_R\text{\^{}}C^{CN}\text{\^{}}C^*{}_R]I_2$ (R = Me **1a**, Et **1b**) were prepared and used to obtain the neutral cycloplatinated complexes $[Pt(C_R{}^*\text{\^{}}C^{CN}\text{\^{}}C_R{}^*)Cl]$ (R = Me **2a**, Et 2**b**) with the NHC acting as a tridentate pincer ligand. Then, substitution of the chloride by carbazole and cyanide rendered complexes **3** and **4**, respectively. Their structural and photophysical properties are mostly determined by the biscarbene pincer fragment. However, the steric and electronic properties of the ancillary ligands are also a shaping factor in the molecular aggregation of the Pt(II) complexes, and therefore in the emitting properties. In consequence, the Cl- and CN-derivatives displayed a rich emissive behavior that was concentration- and excitation wavelength-dependent. This allowed changing the emission color from blue when the dominant emitting state was ^{3}ILCT/^{3}MLCT to white and even orange if additional low-energy emissions rose due to the formation of excimers/aggregates. On the other hand, the bulky Cbz substituent with strong electron donating properties provokes a change in the nature of the emissive state ^{3}L′LCT [π(Cbz) → π*(C*^C^C*)]/^{3}L′MCT [π(Cbz) → d(Pt)] and avoids any aggregation between the platinum molecules. The studied complexes were used as emitters in OLEDs. The emission color of **2b**- and **4b**-based OLEDs could be easily tuned to cover the bluish-green to orange region of the chromaticity diagram by balancing the relative contributions of the vibronic and excimer-like emission. This was achieved *via* modifying the thickness of the non-doped EML – a simple, fast and cost-effective approach. Devices with a 0.3 nm-thick **4b** EML reached a maximum external quantum efficiency of 8.08% and a reduced efficiency roll-off, while devices with a 0.1 nm-thick layer reached a peak luminance of 34 071 cd m^{-2} and a lifetime of 46 minutes at an initial luminance of 245 cd m^{-2}.

Conflicts of interest

There are no conflicts to declare.

Data availability

The data supporting this article have been included as part of the ESI.†

Acknowledgements

This work was supported by the Spanish Ministerio de Ciencia Innovacion y Universidades/FEDER (Grant PID2021-122869NB-I00 funded by MICIU/AEI/10.13039/501100011033 and ERDF/EU) by the Gobierno de Aragon (Grupos E17_23R: Química Inorgánica y de los Compuestos Organometálicos). P. C. is grateful to the University of Zaragoza for a research contract (Programa Investigo 023-56). The authors also acknowledge the Centro de Supercomputación de Galicia (CESGA) for generous allocation of computational resources. This project has been partly funded by the European Union Horizon 2021 research and innovation programme under grant agreement no. 101073045 (TADFsolutions).

Notes and references

1 X. Cai and S.-J. Su, Marching Toward Highly Efficient, Pure-Blue, and Stable Thermally Activated Delayed Fluorescent Organic Light-Emitting Diodes, *Adv. Funct. Mater.*, 2018, **28**, 1802558.

2 G. Li, X. Zhao, T. Fleetham, Q. Chen, F. Zhan, J. Zheng, Y.-F. Yang, W. Lou, Y. Yang, K. Fang, Z. Shao, Q. Zhang and Y. She, Tetradentate Platinum(II) Complexes for Highly Efficient Phosphorescent Emitters and Sky Blue OLEDs, *Chem. Mater.*, 2020, **32**, 537–548.

3 H. Yersin, A. F. Rausch, R. Czerwieniec, T. Hofbeck and T. Fischer, The triplet State of Organo-Transition Metal Compounds. Triplet Harvesting and Singlet Harvesting for Efficient OLEDs, *Coord. Chem. Rev.*, 2011, **255**, 2622–2652.

4 H. Amouri, Luminescent Complexes of Platinum, Iridium, and Coinage Metals Containing N-Heterocyclic Carbene Ligands: Design, Structural Diversity, and Photophysical Properties, *Chem. Rev.*, 2023, **123**, 230–270.

5 W.-P. To, Q. Wan, G. S. M. Tong and C.-M. Che, Recent Advances in Metal Triplet Emitters with d6, d8, and d10 Electronic Configurations, *Trends Chem.*, 2020, **2**, 796–812.

6 J. Liu, T.-L. Lam, M.-K. Sit, Q. Wan, C. Yang, G. Cheng and C.-M. Che, Pure blue phosphorescent platinum(II) emitters supported by NHC-based pincer type ligands with unitary emission quantum yields, *J. Mater. Chem. C*, 2022, **10**, 10271–10283.

7 A. Tronnier, U. Heinemeyer, S. Metz, G. Wagenblast, I. Muenster and T. Strassner, Heteroleptic platinum(II) NHC complexes with a C^C* cyclometalated ligand – synthesis, structure and photophysics, *J. Mater. Chem. C*, 2015, **3**, 1680–1693.

8 J. Roy, M. Forzatti, A. Martín, I. Ara, E. Stanzani, S. Jenatsch, H. J. Bolink, S. Fuertes, D. Tordera and V. Sicilia, Surfing the Color Map with Carbazole-Appended Cyclometalated N-Heterocyclic Carbene Pt Complexes and Their Application in Green Organic Light-Emitting Devices, *Adv. Optical Mater.*, 2025, 2500051.

9 T. Fleetham, Z. Wang and J. Li, Efficient deep blue electrophosphorescent devices based on platinum(II) bis(n-methyl-imidazolyl)benzene chloride, *Org. Electron.*, 2012, **13**, 1430–1435.

10 T. Fleetham, J. Ecton, Z. Wang, N. Bakken and J. Li, Single-Doped White Organic Light-Emitting Device with an External Quantum Efficiency Over 20%, *Adv. Mater.*, 2013, **25**, 2573–2576.

11 J. Liu, T.-L. Lam, M.-K. Sit, Q. Wan, C. Yang, G. Cheng and C.-M. Che, Pure Blue Phosphorescent Platinum(II) Emitters

Supported by NHC-based Pincer Type Ligands with Unitary Emission Quantum Yields, *J. Mater. Chem. C*, 2022, **10**, 10271–10283.

12 Z.-L. Zhu, J. Yan, L.-W. Fu, C. Cao, J.-H. Tan, S.-F. Wang, Y. Yun Chi and C.-S. Lee, Peripheral Engineering of Platinum(II) Dicarbene Pincer Complexes for Efficient Blue Hyperphosphorescent Organic Light-emitting diodes, *Mater. Chem. Front.*, 2023, **7**, 3398–3405.

13 Z. Zhang, P. Wu, K. Wang, H. Lin, E. Spuling, R. Xia, Y. Wu, J. Cao, J. Zhang, B. Wei, S. Brase and Z. Wang, Manipulation of Pt···Pt Interaction in Platinum Complex by Methyl Group to Achieve Single-Doped White OLEDs: An Approach to Simulation of Daylight from Dawn until Dusk, *ACS Mater. Lett.*, 2023, **5**, 920–927.

14 V. Sicilia, L. Arnal, A. J. Chueca, S. Fuertes, A. Babaei, A. M. Igual Muñoz, M. Sessolo and H. J. Bolink, Highly Photoluminescent Blue Ionic Platinum-Based Emitters, *Inorg. Chem.*, 2020, **59**, 1145–1152.

15 S. Fuertes, A. J. Chueca, M. Perálvarez, P. Borja, M. Torrell, J. Carreras and V. Sicilia, White Light Emission from Planar Remote Phosphor Based on NHC Cycloplatinated Complexes, *ACS Appl. Mater. Interfaces*, 2016, **8**, 16160–16169.

16 S. Fuertes, L. Mardegan, I. Martínez, S. Ventura, I. Ara, D. Tordera, H. J. Bolink and V. Sicilia, Green Light-Emitting Electrochemical Cells Based on Platinum(II) Complexes with a Carbazole-Appended Carbene Ligand, *J. Mater. Chem. C*, 2022, **10**, 15491–15500.

17 W.-J. Lin, A. R. Naziruddin, Y.-H. Chen, B.-J. Sun, A. H. H. Chang, W.-J. Wang and W.-S. Hwang, Photofunctional Platinum Complexes Featuring N-heterocyclic Carbene-Based Pincer Ligands, *Chem. – Asian J.*, 2015, **10**, 728–739.

18 S. Fuertes, A. J. Chueca and V. Sicilia, Exploring the Transphobia Effect on Heteroleptic NHC Cycloplatinated Complexes, *Inorg. Chem.*, 2015, **54**, 9885–9895.

19 X. Zhang, B. Cao, E. J. Valente and T. K. Hollis, Synthesis, Characterization, Photoluminescence, and Simulations of a CCC-NHC-Supported Pt_2Ag_2 Mixed-Metal Cluster Containing a $PtAg_2$ Metallacyclopropane., *Organometallics*, 2013, **32**, 752–761.

20 A. V. Rozhkov, I. V. Ananyev, R. M. Gomila, A. Frontera and V. Y. Kukushkin, π-Hole···dz2[PtII] Interactions with Electron-Deficient Arenes Enhance the Phosphorescence of PtII-Based Luminophores, *Inorg. Chem.*, 2020, **59**, 9308–9314.

21 J. Kang, R. Zaen, K.-M. Park, K. H. Lee, J. Y. Lee and Y. Kang, Cyclometalated Platinum(II) β-Diketonate Complexes as Single Dopants for High-Efficiency White OLEDs: The Relationship between Intermolecular Interactions in the Solid State and Electroluminescent Efficiency, *Cryst. Growth Des.*, 2020, **20**, 6129–6138.

22 S. V. Baykov, S. I. Filimonov, A. V. Rozhkov, A. S. Novikov, I. V. Ananyev, D. M. Ivanov and V. Y. Kukushkin, Reverse Sandwich Structures from Interplay between Lone Pair—π-Hole Atom-Directed C···dz2[M] and Halogen Bond Interactions, *Cryst. Growth Des.*, 2020, **20**, 995–1008.

23 A. Bondi, van der Waals Volumes and Radii, *J. Phys. Chem.*, 1964, **68**, 441–451.

24 M.-Y. Leung, M.-C. Tang, W.-L. Cheung, S.-L. Lai, M. Ng, M.-Y. Chan and V. Wing-Wah Yam, Thermally Stimulated Delayed Phosphorescence (TSDP)-Based Gold(III) Complexes of Tridentate Pyrazine-Containing Pincer Ligand with Wide Emission Color Tunability and Their Application in Organic Light-Emitting Devices, *J. Am. Chem. Soc.*, 2020, **142**, 2448–2459.

25 L.-K. Li, M.-C. Tang, S.-L. Lai, M. Ng, W.-K. Kwok, M.-Y. Chan and V. W.-W. Yam, Strategies towards rational design of gold(iii) complexes for high-performance organic light-emitting devices, *Nat. Photonics*, 2019, **13**, 185–191.

26 A. K.-W. Chan, M. Ng, Y.-C. Wong, M.-Y. Chan, W.-T. Wong and V. W.-W. Yam, Synthesis and Characterization of Luminescent Cyclometalated Platinum(II) Complexes with Tunable Emissive Colors and Studies of Their Application in Organic Memories and Organic Light-Emitting Devices, *J. Am. Chem. Soc.*, 2017, **139**, 10750–10761.

27 W. B. Connick, V. M. Miskowski, V. H. Houlding and H. B. Gray, Lowest Electronic Excited States of Platinum(II) Diimine Complexes, *Inorg. Chem.*, 2000, **39**, 2585–2592.

28 M. Wrighton and D. L. Morse, Nature of the lowest excited state in tricarbonylchloro-1,10-phenanthrolinerhenium(I) and related complexes, *J. Am. Chem. Soc.*, 1974, **96**, 998–1003.

29 J. S. McCarthy, M. J. McCormick, J. H. Zimmerman, H. R. Hambrick, W. M. Thomas, C. D. McMillen and P. S. Wagenknecht, Role of the Trifluoropropynyl Ligand in Blue-Shifting Charge-Transfer States in Emissive Pt Diimine Complexes and an Investigation into the PMMA-Imposed Rigidoluminescence and Rigidochromism, *Inorg. Chem.*, 2022, **61**, 11366–11376.

30 X. Lv, D. Zheng, F. Wan, Y. Liu, Z. Guo, D. Cao and X. Yang, Pt(II) Complexes Showing Multicolor Emissions from Nanoparticles in Solution and Reversible Grinding- and Heating-Induced Luminescence Switching in Solid State, *Chem. – Eur. J.*, 2025, e202403886.

31 E. L. Williams, K. Haavisto, J. Li and G. E. Jabbour, Excimer-Based White Phosphorescent Organic Light Emitting Diodes with Nearly 100% Internal Quantum Efficiency, *Adv. Mater.*, 2007, **19**, 197–202.

32 G. Cheng, S. C. F. Kui, W.-H. Ang, M.-Y. Ko, P.-K. Chow, C.-L. Kwong, C.-C. Kwok, C. Ma, X. Guan, K.-H. Low, S.-J. Su and C.-M. Che, Structurally Robust Phosphorescent [Pt(O^N^C^N)] Emitters For High Performance Organic Light-Emitting Devices with Power Efficiency up to 126 Lm W−1 and External Quantum Efficiency Over 20%, *Chem. Sci.*, 2014, **5**, 4819–4830.

33 M. Mao, T.-L. Lam, W.-P. To, X. Lao, W. Liu, S. Xu, G. Cheng and C.-M. Che, Stable, High-Efficiency Voltage-Dependent Color-Tunable Organic Light-Emitting Diodes with a Single Tetradentate Platinum(II) Emitter Having Long Operational Lifetime., *Adv. Mater.*, 2021, **33**, 2004873.

34 Y. Xin, M. Mao, S. Xu, K. Tan, G. Cheng, H. Zhang, H. Dai, T. Huang, D. Zhang, L. Duan and C.-M. Che, High-Efficiency, Long-Lifetime and Color-Tunable Hybrid WOLEDs Using a Platinum Complex with Voltage-Dependent Monomer and Aggregate Emission, *Adv. Sci.*, 2025, 2411364.

35 J. H. Lee, C. W. Joo, B. Sung, S.-J. Woo, S. Woo, G. S. Lee, J. Lee and Y.-H. Kim, Highly efficient single emitter white phosphorescent organic light-emitting diodes based on Pt(II) emitters, *J. Mater. Chem. C*, 2023, **11**, 10730–10737.

36 M. C. Gather, A. Köhnen and K. Meerholz, White Organic Light-Emitting Diodes, *Adv. Mater.*, 2011, **23**, 233–248.

37 ANSI C78.374-2015, *Light-Emitting Diode Package Specification Sheet for General Illumination Applications*, NEMA, Arlington, VA, 2016.

38 S. Wu, S. Li, Q. Sun, C. Huang and M.-K. Fung, Highly Efficient White Organic Light-Emitting Diodes with Ultrathin Emissive Layers and a Spacer-Free Structure, *Sci. Rep.*, 2016, **6**, 25821.

39 M. Forzatti, S.-H. Chin, M. A. Hernández-Fenollosa, M. Sessolo, D. Tordera and H. J. Bolink, Organic Light-Emitting Diodes Combining Thick Inorganic Perovskite Hole Transport Layers and Ultrathin Emitting Layers. Organic Light-Emitting Diodes Combining Thick Inorganic Perovskite Hole Transport Layers and Ultrathin Emitting Layers. Adv, *Opt. Mater.*, 2024, **17**, 2401061.

40 Q. Xue, S. Zhang, G. Xie, Z. Zhang, L. Zhao, Y. Luo, P. Chen, Y. Zhao and S. Liu, Efficient fluorescent white organic light-emitting devices based on a ultrathin 5,6,11,12-tetraphenylnaphthacene layer, *Solid-State Electron.*, 2011, **57**, 35–38.

41 S. W. Kang, D. Baek, B. Ju and Y. W. Park, Green phosphorescent organic light-emitting diode exhibiting highest external quantum efficiency with ultra-thin undoped emission layer, *Sci. Rep.*, 2021, **11**, 8436.